Research

Check for updates

Author for correspondence:
R. Giles Harrison
e-mail: r.g.harrison@reading.ac.uk

THE ROYAL SOCIETY
PUBLISHING

Rapid indirect solar responses observed in the lower atmosphere

R. Giles Harrison and Michael Lockwood

Department of Meteorology, University of Reading, Earley Gate, Reading RG6 6BB, UK

iD   RGH, 0000-0003-0693-347X; ML, 0000-0002-7397-2172

Establishing clear evidence of solar-induced lower atmosphere effects is hampered by the small 11-year solar cycle responses, typically swamped by meteorological variability. Strong 27-day cyclic changes are exploited here instead. During the 2007/8 minimum in solar activity, regular 27-day lighthouse-like sweeps of energetic particles crossed the heliosphere and Earth, followed by a burst of solar ultraviolet radiation. Averaging the atmospheric responses at UK sites reveals immediate cooling in the troposphere after the peak energetic particle flux, followed by warming in the stratosphere. Regionally, this is accompanied by zonal wind changes, and temperature changes beneath cloud at the same time. Of two possible rapid distinct routes of solar influence—photochemical (through ozone) and atmospheric electrical (through low level clouds)—the ozone route does not provide a phase-locked response but the electrical route is supported by observed phase-locked thickening of low level clouds. These findings have potential value to weather forecasting.

1. Introduction

Atmospheric changes driven by the sun's variability occur through multiple pathways [1], but the simultaneous solar modulation of multiple parameters such as ultraviolet radiation, total solar irradiance and, inversely, galactic cosmic rays, has made the dominant mechanisms difficult to uniquely identify and quantify [2,3]. The 11-year solar cycle also limits practical measurement consistency to only a few solar cycles, restricting statistical confidence given the great variability in other atmospheric processes. Examining the response to the 27-day solar rotation instead allows many cyclic variations from short measurement periods, during which homogeneity is more readily maintained.

An occasional heliospheric feature strengthening solar rotation effects is a co-rotating interaction region (CIR) [4], resulting from an isolated coronal hole or a localized extension of a polar coronal hole to the heliographic latitude of Earth. CIRs are caused by fast solar wind from the coronal hole interacting with slow solar wind ahead, modulating the galactic cosmic rays (GCR) flux through shock waves and compression regions. Such a GCR modulation occurred in 1996 [5], and a further persistent CIR pattern in 2007/8 allowed solar effects in surface atmospheric electricity to be identified at mid-latitudes [6]. The 2007/8 27-day solar signals were particularly pronounced because the Sun was approaching its lowest minimum in activity since 1901, with an associated increased GCR flux and only one isolated active region remaining on the solar surface (see appendix A). The year-long repeated 27-day heliospheric modulation from the 2007/8 CIR is used here to identify solar-induced meteorological effects in the troposphere and stratosphere.

2. Observed meteorological changes

(a) Surface

Figure 1 motivates investigating solar effects on the lower atmosphere in 2007/8. Data from the Oulu neutron monitor measuring GCR often show strong solar influences [7], and figure 1a shows the interesting period of repeated 27-day oscillations due to the CIR, centred around January 2008. Surface air temperature measurements at Reading (51.44°N, 0.93°W) for the same time are presented in figure 1b, from which 27-day variability is suggested by eye; consistency between observations of traditional liquid-in-glass thermometers and modern electronic sensors discounts possible effects of induced geomagnetic currents, supporting an actual meteorological variation rather than a measurement artefact. The surface wind direction (figure 1c), a quantity particularly sensitive to atmospheric changes [8], also shows possible approximately 27-day variability. From the associated periodograms figure 1d–f, calculated from each of the time series figure 1a–c, 27-day variability is robustly present in the neutron monitor data and less so in the wind direction, but not the near-surface air temperature.

The occurrence of 27-day oscillations has previously been reported in other data, notably cloud [9], from which a coupled surface temperature response could result, but the presence of the 27-day oscillation period alone is insufficient to uniquely confirm a solar origin. The lunar monthly tide, for example, also exhibits similar periodicities, e.g. the mean monthly tide of 27.55 days and the sidereal cycle of 27.3 days. Additional evidence can, however, be provided by considering the phase relationship between the terrestrial changes and the solar variations, found from averaging together (compositing) data around the maxima and minima. For robust features to emerge from this approach, not only is a 27-day oscillation necessary, but the same phase response needs to be repeated over each cycle, i.e. the 27-day variations of both the solar and suspected atmospheric response need to vary consistently together, with a fixed phase relationship. To obtain the maxima and minima times for such averaging, a phase-preserving bandpass filter (passband 25–30 days) is used to smooth the neutron monitor data to identify consecutive maxima and minima, as previously [6]. These derived dates of maxima and minima are marked on the time series of figure 1a–c as (red) dashed lines and (blue) dotted lines respectively, and are provided in table 1. (Their mean interval is 27.0 days.)

By averaging on the neutron maxima and minima during the period of the CIR (not shown), the surface air temperature at Reading is found to rise before the maxima and fall after it. (The median of the temperature anomalies for the prior 14 days is +0.31°C, and −0.28°C for the subsequent 14 days, which a Wilcox test shows are not the same, with a probability p of occurrence by chance $p < 0.02$.) The surface wind direction turns clockwise and then anticlockwise around the CIR maxima (not shown), with its most northerly direction on the day of the maximum. Both occur within considerable variability, but the presence of systematic changes at all encourages further investigation. As changes in near-surface properties are usually linked
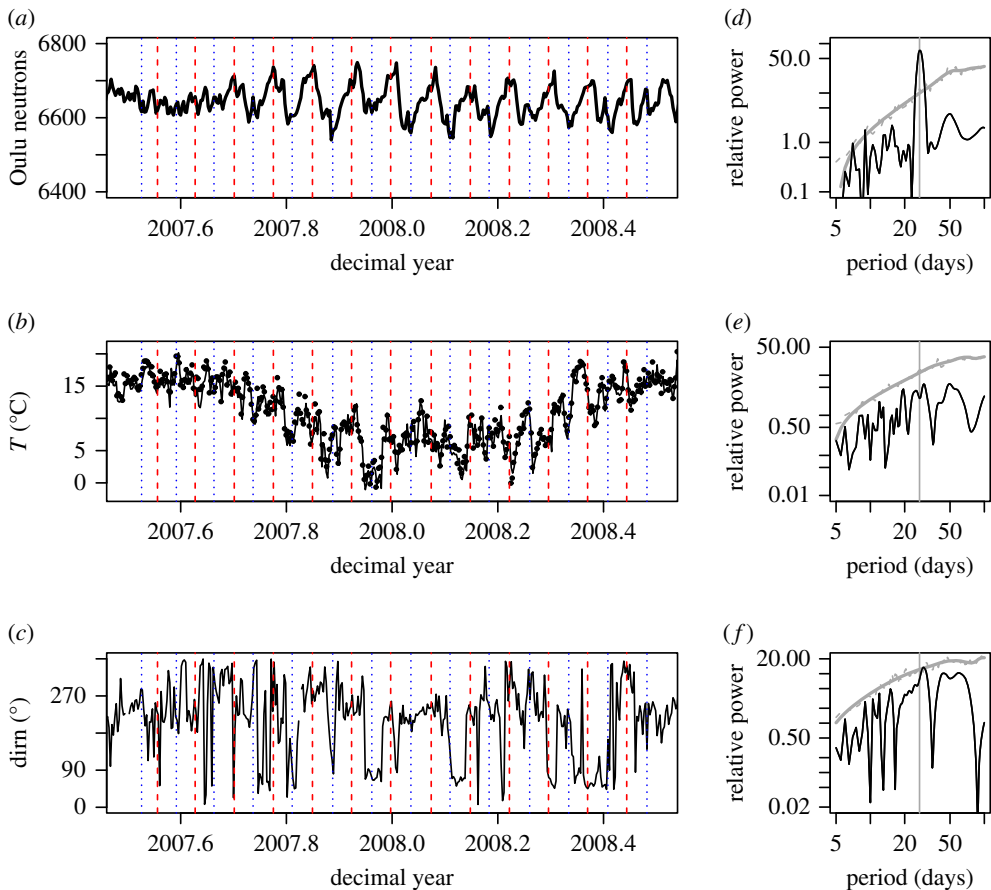
Figure 1. Time series of daily averages of (*a*) Oulu neutron monitor count rate, (*b*) Reading air temperature (manual observations as points, automatic observations as lines) and (*c*) Reading wind direction, with the maxima (red dashed lines) and minima (blue dotted lines) of 25- to 30-day band-passed data from (*a*) marked. (*d*), (*e*), (*f*) show the Lomb periodograms for (*a*), (*b*) and (*c*) (East–West component) respectively, for detrended data with a cosine bell taper (taper = 0.5) applied. (On the periodograms, the vertical grey line marks periodicity at 27 days; the thick grey line marks the 95% confidence limit obtained by assuming an autoregressive process (AR1) of the same autocorrelation.) (Online version in colour.)

to vertical meteorological changes generating temperature or pressure gradients, these small hints of atmospheric changes phase-locked with solar-induced variations are pursued further by examining the contemporary UK atmospheric soundings obtained from radiosondes.

(b) Upper air

During the 2007/8 CIR period, soundings were made twice-daily from the UK Met Office sites at Herstmonceux (51.48°N, 0°W), Camborne (50.22°N, 5.33°W) and Lerwick (60.14°N, 1.18°W). In data from each site, a 27-day pattern of alternate tropospheric warming and cooling is apparent in the temperature anomalies, and the opposite pattern in the stratosphere, made clear through compositing. Figure 2 shows the phase relationship in the vertical air temperature anomalies around the neutron (CIR) maxima. All three sites show the same distinctive chequerboard pattern, with positive tropospheric temperature anomalies before the neutron maxima, and positive stratospheric temperature anomalies soon afterwards. Values lying outside the inner 95% of values at the same height level are marked, which support the chequerboard pattern being an exceptional feature.

Table 1. Dates of derived maxima and minima in the 2008 CIR period.

minima				maxima			
decimal year	year	day	mon	decimal year	year	day	mon
2007.526	2007	12	7	2007.556	2007	23	7
2007.592	2007	5	8	2007.627	2007	18	8
2007.663	2007	31	8	2007.701	2007	14	9
2007.737	2007	27	9	2007.775	2007	11	10
2007.811	2007	24	10	2007.849	2007	7	11
2007.888	2007	21	11	2007.923	2007	4	12
2007.962	2007	18	12	2007.997	2007	31	12
2008.036	2008	14	1	2008.074	2008	28	1
2008.11	2008	10	2	2008.148	2008	24	2
2008.184	2008	8	3	2008.222	2008	22	3
2008.26	2008	5	4	2008.296	2008	18	4
2008.334	2008	2	5	2008.373	2008	16	5
2008.408	2008	29	5	2008.447	2008	12	6
2008.482	2008	25	6				

4

royalsocietypublishing.org/journal/rspa   *Proc. R. Soc. A* **476**: 20200164

The phase-locked temperature responses to the timings of the neutron variations point to an effect of the solar fluctuations on the stratosphere and troposphere.

3. Potential origins for the observed changes

The temperature responses observed in the troposphere around the CIR maxima and minima occur rapidly, in days, arguing against downward dynamical propagation of signals from the stratosphere, which typically takes weeks [10,11]. Evidence for lunar tidal effects on the polar jet stream has also been presented [12]. Possible rapid transfer mechanisms are, however, limited, such as a direct radiative response through ozone changes, or ion absorption [13], or, in the troposphere where the slight electrical conductivity allows charge from energetic particles to persist, via electrical coupling into layer cloud droplet microphysics (e.g. [14]). These possible stratospheric and tropospheric responses are now considered separately.

(a) Stratospheric

Stratospheric radiative responses to solar changes can arise through ozone changes, such as ozone destruction by solar energetic particles [1], or enhanced photochemical production from oxygen dissociation by solar radiation at wavelengths around 200 nm. Figure 3 contrasts these possible contributory factors, showing variations in energetic protons observed by the GOES-11 satellite detector (figure 3*a*), and ultraviolet (UV) radiation measured by the SOLSTICE instrument on the SORCE satellite, integrated from 170 to 220 nm to represent the ozone-forming wavelengths (figure 3*b*). Both quantities show regular modulation during the CIR period, with the energetic protons' variations closely correlated with the timing of the neutron maxima and minima.

Exploring the UV changes further, figure 3*c* presents the time series of the UV spectral variation, showing that not all solar rotations provide identical UV modulation, and that the major UV pulses occur between the neutron maxima and minima. To consider whether there is a UV-driven effect on the stratospheric ozone, figure 3*d* shows daily variations in the stratospheric ozone column at Lerwick and Reading, from Dobson and Brewer spectrometers respectively, and
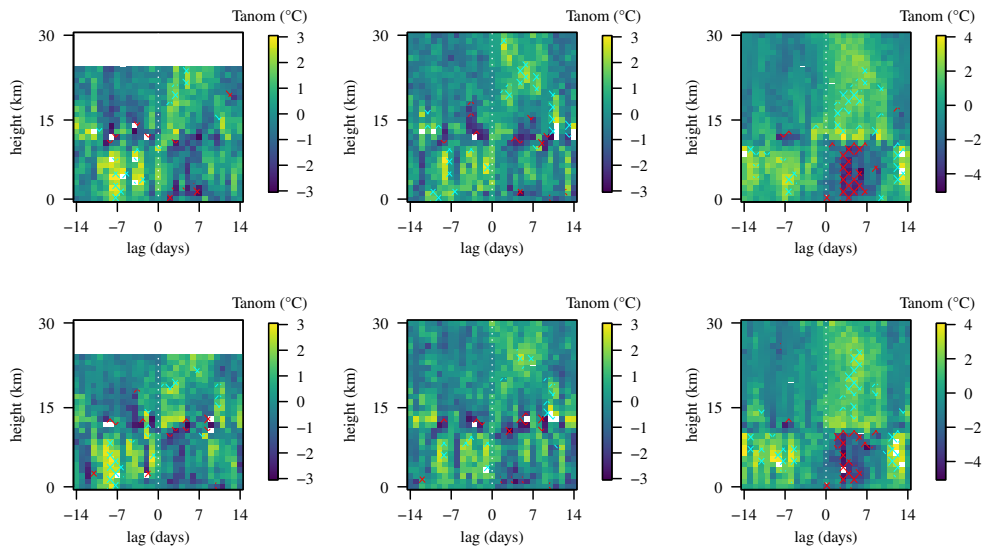
Figure 2. Composites of temperature anomalies (after seasonal detrending) averaged to 1 km height layers around the neutron maxima of table 1 for (left col) Herstmonceux, (centre col) Camborne and (right col) Lerwick, from daily radiosonde launches at 11 UTC (upper row) and 23 UTC (lower row). (Hatching shows values with 95% significance or greater, and blank regions mark values beyond the range of the colour scale. The Herstmonceux ascents only reach 24 km.) (Online version in colour.)

the weekly integrated ozone sounding at Lerwick. Beyond the strong seasonal variation, changes in ozone column associated with the solar- UV variations are not clearly present.

Nevertheless, to consider this possibility further, composites of the satellite-determined UV variations and Lerwick ozone have been generated, around the CIR maxima and minima (figure 4). From these, the peak-to-peak variation in integrated UV irradiance is about $3 \, \text{mW m}^{-2}$ (approx. 0.5%), reaching its maximum 7 days after CIR maximum. No column ozone destruction is evident after the neutron maxima, which restricts the possible stratospheric ozone effects to photochemical production. (A similar data analysis, but using a lunar signal and the AO index, following Best & Madrigali [12], yielded no significant changes.) Despite compositing the data, ozone column variations at Lerwick are still not strongly evident, other than a small decrease or increase across the CIR minimum and maximum which is within the normal variability. Quantitatively, from the ozone formation enthalpy ($142.7 \, \text{kJ mol}^{-1}$) and neglecting transport and mixing, $3 \, \text{mW m}^{-2}$ irradiance for 12 h would be expected to yield about 2 Dobson Units (DU) of ozone daily, or to add about 1% to the column. Modelled ozone-induced stratospheric temperature changes [15] showed that a 1% increase in ozone at 50°N and approximately 100 hPa (20 km) would cause a local warming of approximately 0.4 K, hence, if sustained over 5–10 days, a small ozone increase could contribute to the stratospheric temperature increase comparable with that observed.

The absence, however, of substantial phase-locked signals in the ozone column suggests that ozone changes alone are unlikely to fully account for the immediate meteorological changes observed, and therefore tropospheric effects, potentially propagating upwards, are now considered further.

(b) Tropospheric

The large tropospheric temperature changes observed are unlikely to result solely from direct radiative changes in the stratosphere, which in any case appear small. Stratospheric warming induced by the solar cycle can, however, generate lower troposphere zonal wind changes [2,16] or modifications of planetary waves [16], and sudden stratospheric warmings in the Northern
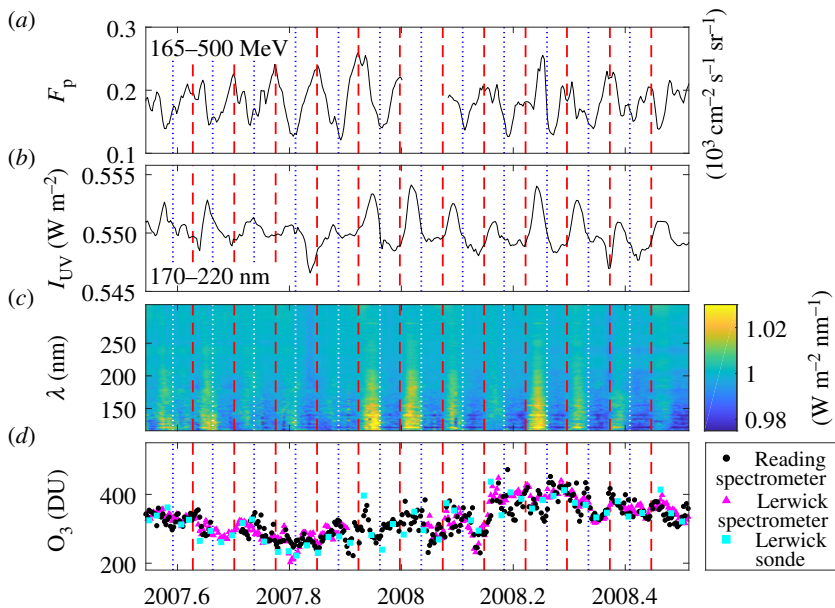
Figure 3. Daily time series of (*a*) energetic (165–500 MeV) protons detected by the GOES11 satellite, (*b*) the integrated UV measured by SORCE at wavelengths between 170 and 220 nm and (*c*) its relative spectral variation, (*d*) ozone column time series obtained from surface spectrometers at Lerwick and Reading, and the Lerwick ozonesonde. (Online version in colour.)

Hemisphere can yield persistent mid-troposphere wind changes [17]. This provokes investigating the tropospheric temperature changes as associated with wind direction changes, hinted at in figure 1*c* in the analysis of the Reading surface data.

Wind profiles from the Lerwick soundings are accordingly presented in figure 5, as composites, in which a strong effect is apparent. These show, on average, that the meridional flow shows little change, except in the stratosphere a few days after the maxima (figure 5*a*), but that the mid-tropospheric zonal wind changes approximately symmetrically in the few days around the neutron maxima (figure 5*b*). In wind vector terms, this moves the tropospheric airflow from south-westerly (warmer) to more north-easterly (cooler) (figure 5*c*). Near the surface, as for the surface observations at Reading, the wind direction becomes northerly around the time of the maximum. A rapid change in wind direction would account for the almost immediate tropospheric temperature changes observed, with a later change in the stratosphere (e.g. Figure 5*a*) associated with either the later UV maximum (figure 4*b*) or, possibly, a tropospheric disturbance propagating upwards.

Origins for this wind direction change are now considered further. Firstly, there is the possibility that the effect is more widespread regionally. Meteorological reanalyses are suitable for studying this, as they harmonize an extensive range of observations with numerical forecasts to provide, retrospectively, an optimized description of the atmosphere. For example, the NCEP reanalysis [18], provides atmospheric data throughout the 2007/8 CIR period at daily resolution. To investigate the regional aspects, composites using the NCEP reanalysis data have been made (figure 6) for 50°N to 90°N and from 90°E to 90°W, which include the positions of the UK sites. As for the Lerwick site of figure 5 at 60°N, figure 6 shows that the mean zonal wind is strengthened (more positive) at about 10 km during the CIR maxima compared with the CIR minima. The wind changes found for Lerwick are therefore part of a regional change. In addition, the mean zonal wind through the depth of the troposphere nearer the pole and at lower levels to about 70°N is also strengthened at CIR maxima compared with CIR minima. This also differs from the long-term climatology, generated from the same dates as the CIR maxima.
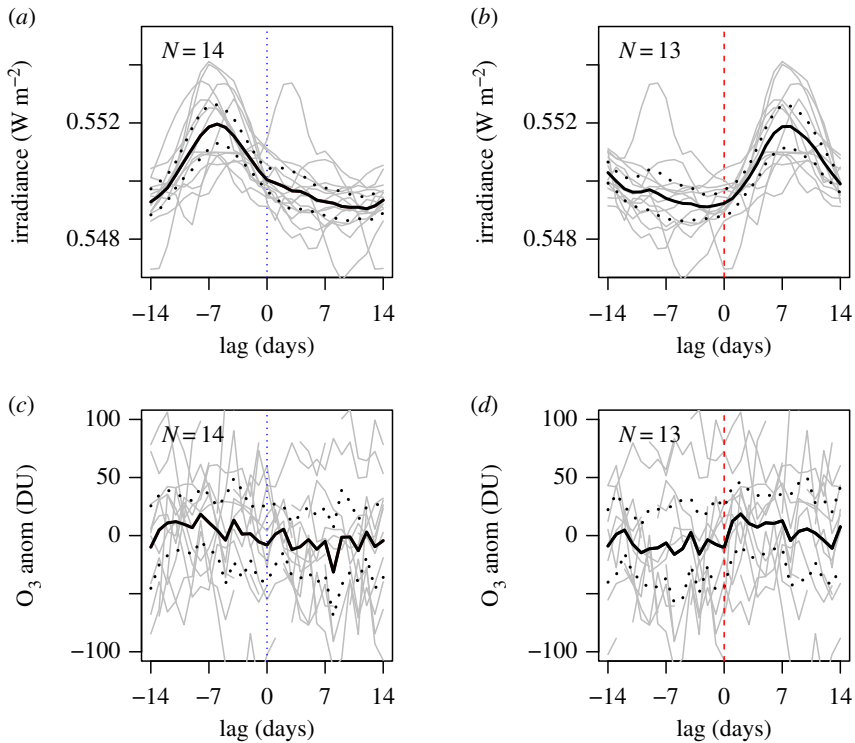
Figure 4. Composites of (*a*) and (*b*) integrated UV irradiance from SORCE (170–220 nm), and (*c*) and (*d*), Lerwick column Ozone anomalies, as medians (thick black lines) around minima (left-hand column) and maxima (right-hand column) in the neutron time series. The dashed lines show 95% confidence limits on the medians, and the thin grey lines data from the individual intervals. (Online version in colour.)
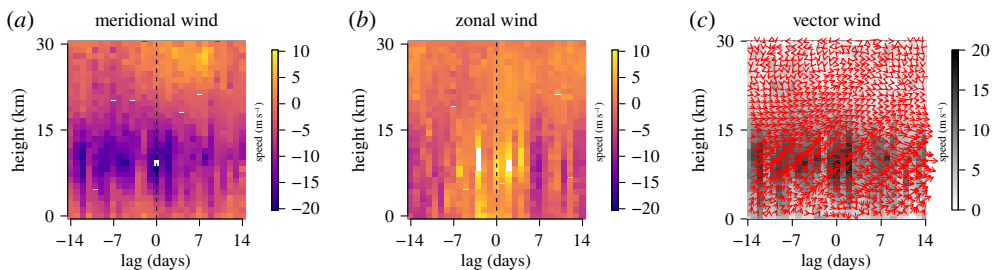

Figure 5. Profile of mean wind speeds obtained from the Lerwick radiosondes at 23UTC, composited around neutron maxima for the (*a*) meridional and (*b*) zonal directions. (*c*) shows the vertical profile of the vector wind direction for the same times, with the arrow length proportional to the mean wind speed (also shown through the background colour scale). (Online version in colour.)

The zonal wind is closely related to the horizontal thermal gradient, through the thermal wind balance (e.g. [19]). An associated change in the temperature pattern between CIR max and CIR min is therefore expected. Further composites derived from NCEP reanalysis temperature data are provided in figure 7. These demonstrate a difference in the thermal structure between CIR maxima and minima; figure 7*c* indicates that the cold and warm anomalies around 70°N are the more robust aspect.
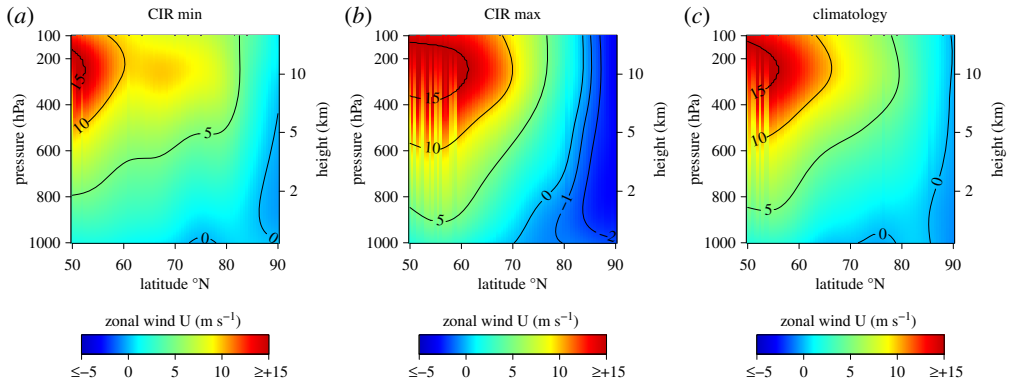
Figure 6. Latitudinal profile of the composite mean zonal wind from 90°E to 90°W, made from the NCEP reanalysis during (*a*) the 2007/8 CIR minima and (*b*) maxima and (*c*) the climatological mean on the same dates as those of the CIR maxima but across 1981–2010. (Online version in colour.)
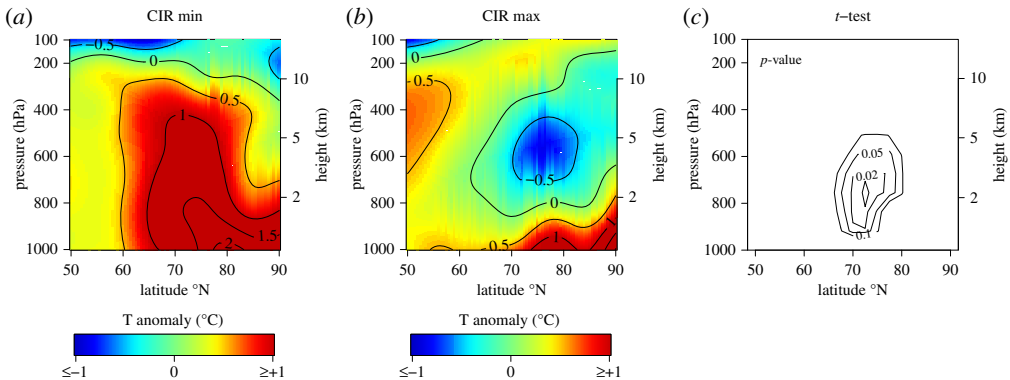

Figure 7. Composites of the latitudinal profile of air temperature anomalies (compared with 1981–2010) at 90°E to 90°W from the NCEP reanalysis for the 2007/8 CIR period and smoothed, for (*a*) CIR minima and (*b*) CIR maxima. (*c*) shows the probability (*p*-value) from a *t*-test (using the unsmoothed data), that the difference arises from chance. (Online version in colour.)

The low-level warm anomaly around 70°N to 80°N could be related to low cloud, acting to trap outgoing radiation and restrict the diurnal temperature range. Accordingly, the NCEP reanalysis has been examined for cloud-related quantities. Figure 8 shows a further composite, but for the relative humidity (RH), in which, for air temperatures less than 0°C, the RH has been evaluated with respect to ice. The NCEP RH data is provided up to 300 hPa, at approximately 100 hPa steps: as this is a relatively smooth field it has been interpolated onto 5 hPa steps to provide greater resolution. It is apparent that, compared with the RH field for the CIR minima (figure 8*a*), moist air around 70°N to 80°N deepens at CIR maxima (figure 8*b*). The increased depth of moist air during the CIR maxima is unusual, as it differs from the climatological mean 1981–2010 calculated for the same dates (figure 8*c*). Values of RH (with respect to ice) greater than about 80% are associated with cloud, although a precise threshold is difficult to establish [20]. The increased moist air depth can therefore be interpreted as a change in cloud between 75°N to 85°N, indicating increased low cloud thickness from about 1 km during CIR minima to about 2 km during CIR maxima. This can be associated with the warm anomaly apparent at the same position in figure 7*b*.

In summary, during CIR maxima compared with CIR minima, the midlatitude to pole Northern Hemisphere troposphere between 90°E to 90°W shows (i) changes in the wind structure
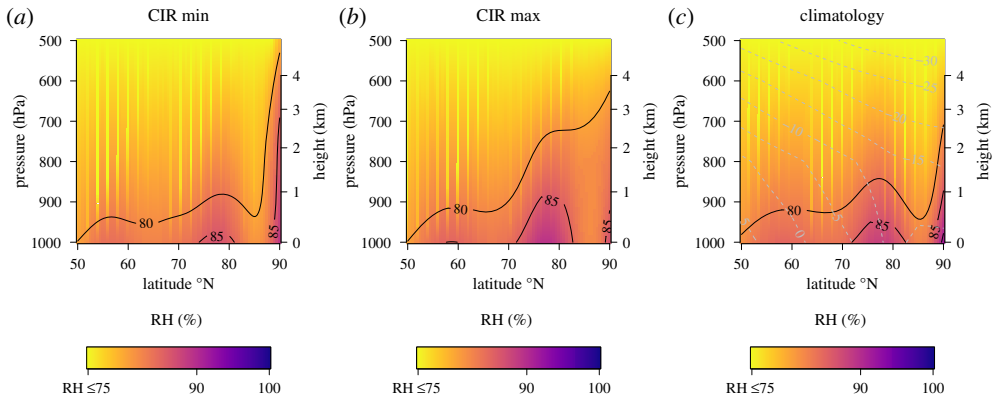
Figure 8. Composite mean values of the latitudinal vertical profile of relative humidity (calculated with respect to ice for air temperatures less than 0°C) at 90°E to 90°W from the NCEP reanalysis for the 2007/8 CIR period, during (*a*) CIR minima and (*b*) maxima. (*c*) shows the mean value of RH from the same dates as for the maxima, but across all years 1981–2010. Dashed lines in (*c*) show the climatological mean air temperature (in Celsius). (Online version in colour.)

different from the climatology, (ii) a low level thermal change around 70°N, and (iii) an increased thickness of low level cloud, again differing from climatology.

(c) Global

Effects are now considered at the larger scale, again using the NCEP reanalysis data. Figure 9 shows global composites of low level (approx. 725 m) air temperature anomalies calculated using the same CIR maxima and minima of table 1. Figure 9*a*,*b* shows positive temperature anomalies in both polar regions during the CIR maxima, compared with the CIR minima. These figures also include an estimate of the presence of cloud (derived from the relative humidity data for the same times) immediately above the temperature determination region. From these it is apparent that many of the warm anomalies are beneath cloud, and that the principal temperature anomalies occur at high latitudes in both hemispheres.

Because of the seasonal timing of the CIR maxima and minima (table 1), many of the maxima considered in the analysis of figure 9*a*,*b* occur during the Northern Hemisphere winter. Figure 9*c* investigates this further, showing the composite of near-surface air temperature anomalies for the four CIR maxima during December-January-February (DJF) only. This closely resembles the pattern for the whole period of the data shown in figure 9*b*, and therefore it is likely that an appreciable contribution to the whole composite arises during the Northern Hemisphere winter. Figure 9*d* shows the associated day length during the same time, from which it is apparent that the regions of DJF positive temperature anomalies occur despite seasonally restricted daylight.

4. Discussion

Atmospheric changes occur between CIR maxima and minima, which are apparently related to near-surface temperature changes, particularly at high latitudes. The changes are phase related with solar-induced changes in energetic particles, but not with solar UV changes, which show a different phase response. The similar response apparent in both hemispheres at high latitudes further supports the action of energetic particles as the route by which the solar changes influence the lower atmosphere, due to the reduced geomagnetic shielding to energetic particles near the poles.

In the troposphere, energetic particles have previously been suggested to influence clouds. Two major routes have been proposed to provide the link between ionization and clouds:
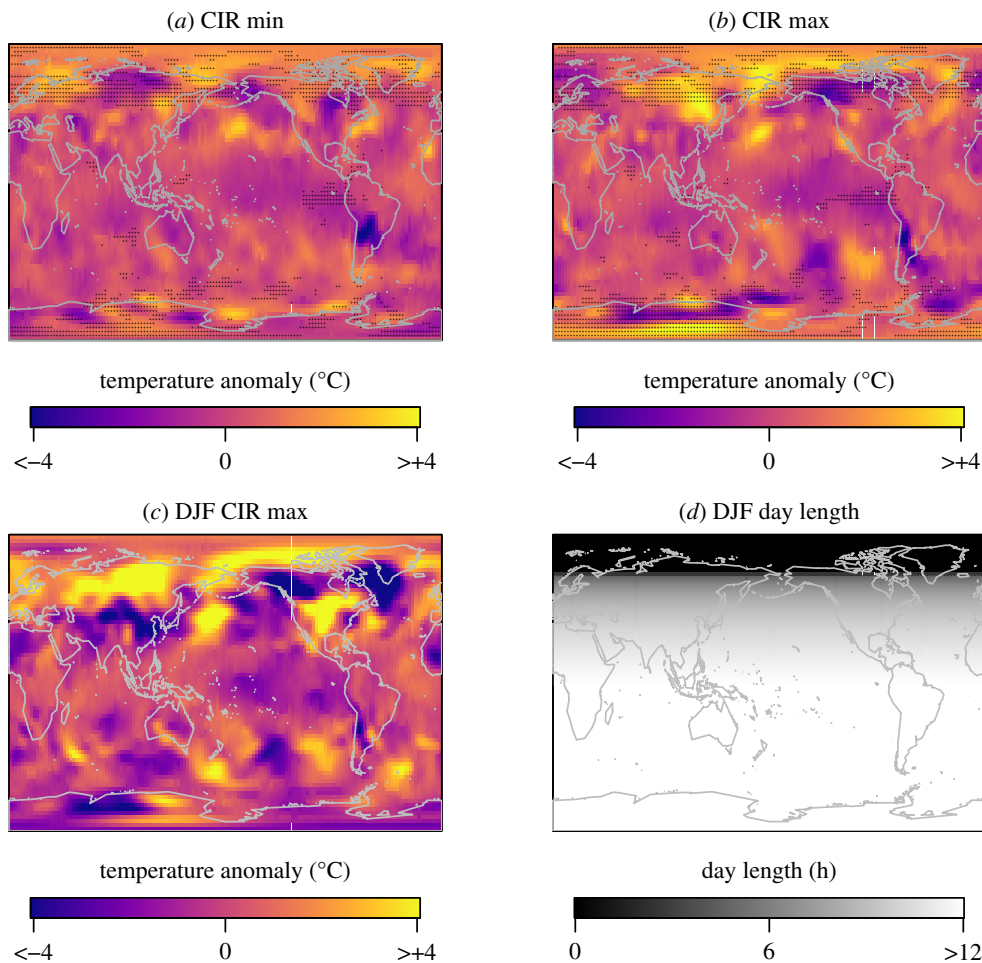
Figure 9. Global daily air temperature anomalies (from the 1981–2010 climatology) at 925 hPa (approx. 750 m), composited for 2007–2008 dates of (*a*) CIR minima and (*b*) CIR maxima in the neutron time series. Stippling indicates cloud (considered as relative humidity with respect to ice greater than 80%) immediately above, at 850 hPa (approx. 1500 m). (*c*) Composited 925 hPa daily air temperature anomalies from the four CIR maxima during December-January-February (DJF). (*d*) Median day length for DJF. (Online version in colour.)

(i) through ion-induced generation of cloud condensation nuclei (CCN) or (ii) electrically induced droplet changes in layer clouds (e.g. [21]). The CCN nucleation mechanism is a weak effect (e.g. [22]), and unlikely to strongly contribute in the situations considered because the Northern Hemisphere warming anomalies identified at CIR maxima are dominated by winter, figure 9*c*, when there would be restricted daylight (figure 9*d*) available for the required photochemical sulphuric acid production. The second mechanism influencing the microphysics of low level layer clouds, through enhanced global circuit current flow causing charging at their upper and lower horizontal edges, has been extensively discussed (e.g. [1,2,14,23,24]) but the possible responses have not yet been fully disambiguated and quantitatively evaluated [25]. This deserves further consideration in the light of these results because the cloud response observed (thickening of Northern Hemisphere cloud, figure 8*b*) at CIR maxima occurs when the global circuit current also increased [6], and the global thermal anomalies of figure 9*b* are mostly associated with low cloud.

Taking these phenomena together, a causal chain (summarized in figure 10) can be constructed for an energetic particle influence on the lower atmosphere. This is through the global
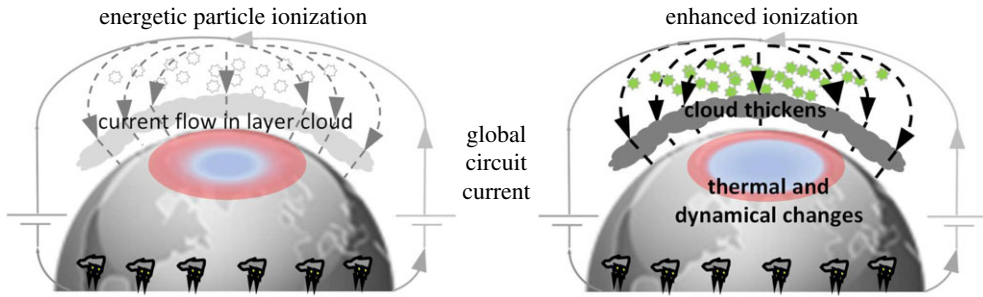
Figure 10. Proposed causal linkage of solar energetic particles effects into the troposphere. (Left) Current flow in the global atmospheric electric circuit. This is driven principally by charge separation in equatorial regions, flowing through the conductive upper atmosphere and returning through the vertical conduction current density, some of which passes through extensive layer clouds in the lower troposphere. (Right) During enhanced ionization from solar energetic particles, the upper atmosphere becomes more electrically conductive at high latitudes and the current passing through layer clouds increases. Thickened low level clouds modify the local thermal structure of the troposphere, with dynamical changes influencing wind directions. (Online version in colour.)

atmospheric electric circuit, in which solar modulation of energetic particles modulates the current flowing through extensive stratiform clouds at high latitude. With increased current, thickening of low clouds through electrical influence on the droplet microphysics would act to increase the near-surface temperature. The thermal structure of the troposphere would change, modifying the thermal gradient between the pole and mid-latitudes. The thermal structure and circulation are coupled, bringing local temperature fluctuations in response to changes in wind directions. Such a mechanistic route through global circuit changes would be rapid, essentially communicated immediately where layer clouds are present, and through which current flows. These considerations are consistent with the immediate lower troposphere temperature changes apparent in figure 2, the observed low cloud thickening and zonal wind changes, and, potentially, the somewhat later temperature response observed in the stratosphere.

5. Conclusion

This work demonstrates an association of a solar influence with rapid changes in the atmosphere's thermal structure, through effects initiated in the lower troposphere. Further, because the peak intensities in solar-driven energetic particles and UV radiation changes were separated by many days, their different transient effects are distinguishable. This shows that the UV variations cannot be the sole source of the tropospheric changes observed, as energetic particle changes are also phase-locked with the tropospheric changes. A rapid transfer mechanism is necessary to drive these changes, for example through modifying current flow through extensive layer clouds, with associated effects on the cloud microphysics. Although in this work special heliospheric conditions were necessary to separate the solar indirect effects explicitly, the indirect route of solar effects identified will continuously contribute to natural variability in the climate system.

Representing the atmospheric response to solar fluctuations in numerical models through this mechanism offers new potential in weather forecasting, and may help account for unexpected sources of atmospheric variability in the approaching solar minimum.

Appendix A

The minimum in solar activity between solar cycles 23 and 24 was the deepest and longest seen since that around 1910. The open solar flux, as deduced from measurements of the near-Earth interplanetary magnetic field (with kinematic correction for folded flux and averaged over solar Carrington Rotation periods [26]), reached a minimum value of 1.174×10^{14} Wb midway through 2009: the lowest such value since such observations began in 1963. Cosmic ray fluxes detected by high-latitude neutron monitors (such as that at Oulu) consequently reached their greatest values since those observations began, which was again in the early 1960s [27]. In the approach to this minimum there was an extended interval of little or no sunspot activity in which the minimal solar activity occurring set up a remarkably stable interval showing strong oscillations at the solar rotation interval of near 27 days. The mean solar rotation period is the 'Carrington Rotation' (CR) interval of 25.38 days with respect to the fixed stars [28], which, when added to Earth's orbital motion gives a mean synodic period of 27.2753 days as seen from Earth. Remarkably, regular oscillations with the CR period persist in some solar and heliospheric parameters for over 13 solar rotations, which is a full year. The associated main paper deals with some consequences of these oscillations for the terrestrial atmosphere; here we provide a fuller explanation of their origin.

In each panel of figure 11 the left-hand plot gives the time series of a solar or heliospheric parameter with the start of each solar Carrington Rotation (CR) period marked by a vertical mauve line. The right-hand plots give a composite for that parameter (from a 'Chree' or superposed epoch analysis) showing the variations for each CR as a function of the phase of each CR interval, ϕ_{CR}, as a grey line and their average as the black line. The units for each parameter are given in parentheses to the right of each panel. The top panel gives ϕ_{CR}. Figure 11*b* shows the counts recorded by the Oulu neutron monitor, revealing consistent peaks in galactic cosmic ray fluxes (GCRs) just after the start of each CR and a minimum just after midway through each CR. The instrument at Oulu is sensitive to particles of energy above about 2 GeV. This is not a terrestrially or atmospherically generated phenomenon because matching oscillations are seen in energetic proton fluxes observed by the GOES-11 spacecraft in geostationary orbit (figure 11*c*). The proportional variation of the proton flux, $100.(Fp - \langle Fp \rangle)/\langle Fp \rangle$ is greatest for the highest energy channel (165–500 MeV: shown by the black line) and weakens for lower energy bands (the time variation for the 4–9 MeV and the average composite are shown in green). This shows that the protons seen by GOES-11 are not Solar Energetic Particles accelerated at shocks in the heliosphere (e.g. [29]) but the lower energy tail of the GCRs detected by neutron monitors.

The cause of the 27-day modulation of GCR fluxes can be understood from the near-Earth heliospheric data and data from solar magnetograms. The near-Earth IMF B_X component (figure 11*d*) shows an exceptionally stable two-sector structure with 'Toward' (the Sun, i.e. $B_X > 0$) IMF at ϕ_{CR} between about 65° and 220° and 'Away' (the Sun, i.e. $B_X < 0$) for the rest of the CR. This means that Earth crosses the heliospheric current sheet twice in each CR at around these ϕ_{CR} values and the HCS is embedded in the streamer belt. Figure 11*e* shows that either side of the more rapid of the two Bx reversals (at around $\phi_{CR} = 220°$) are peaks in the solar wind speed,
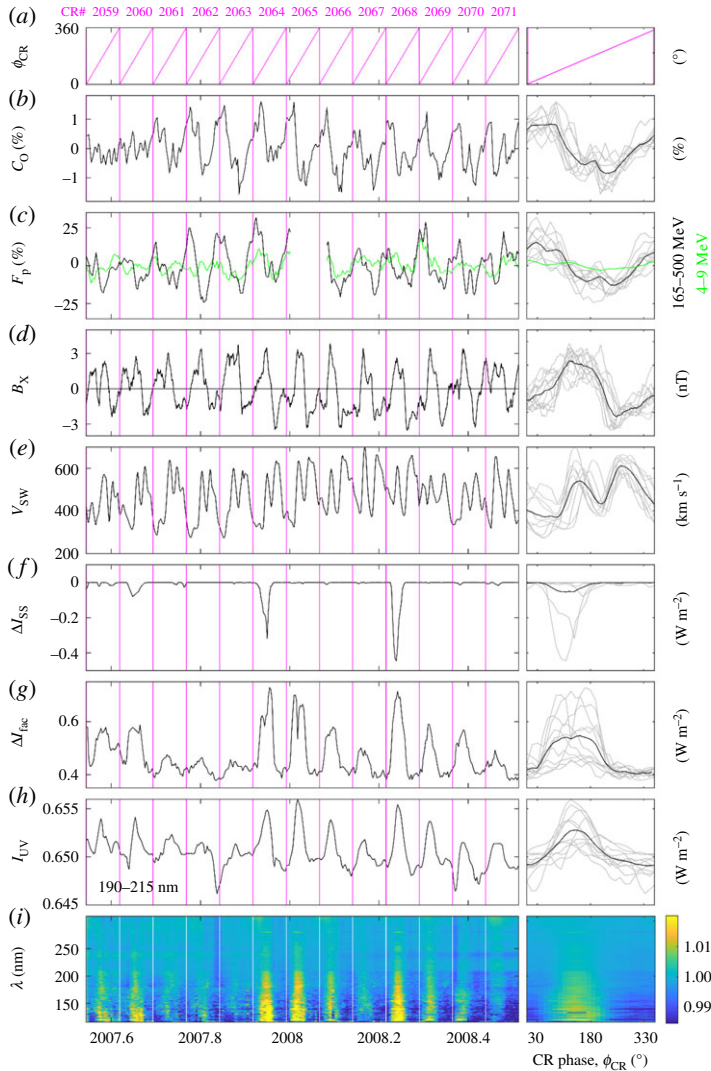
Figure 11. Solar and heliospheric data from the activity minimum between solar cycles number 23 and 24. Left-hand panels provide time series with the start of each solar Carrington Rotation (CR) period marked by a vertical mauve line. The plot covers 13 CRs starting at the start of CR number 2059 (09:07:44 UT on 18 July 2007) and ending at the end of CR number 2071 (23:40:26 UT on 6 July 2008). The right-hand plots give a composite for that parameter (from a 'Chree' or superposed epoch analysis) showing the variations for each CR as a function of CR phase, ϕ_{CR}, as a grey line and their average as the black line. The units for each parameter are given in parentheses to the right of each panel. From top to bottom panels are for: (*a*) the CR phase, ϕ_{CR}: the designated CR numbers are given in mauve along the top of the panel; (*b*) the counts C_O recorded by the neutron monitor at Oulu; (*c*) the ratio of the integral number flux of protons F_p to the mean value over the interval $\langle F_p \rangle$, detected by the GOES-11 satellite—the black line is for 165–500 MeV and the green line for 4–9 MeV; (*d*) the sunward radial component of the near-Earth interplanetary magnetic field, B_X, as measured by the WIND and ACE spacecraft; (*e*) the solar wind speed, V_{SW}, as measured by the WIND and ACE spacecraft; (*f*) the sunspot darkening factor calculated from magnetograph data using the SATIRE model of total solar irradiance, ΔI_{SS}; (*g*) the facular brightening factor calculated from magnetograph data using the SATIRE model of total solar irradiance, ΔI_{fac}; (*h*) the integrated UV irradiance over the ozone-effective wavelength band of 190–215 nm from the XPS, SOLSTICE, and SIM instruments on the SORCE spacecraft, I_{UV}. The bottom panel (*i*) shows the SORCE UV spectral irradiance data in wavelength-time spectrogram format for wavelengths between 115 and 310 nm; the coloured pixels give the fractional deviation of the irradiance at each wavelength λ from the overall mean for the whole interval for that particular λ. (Online version in colour.)
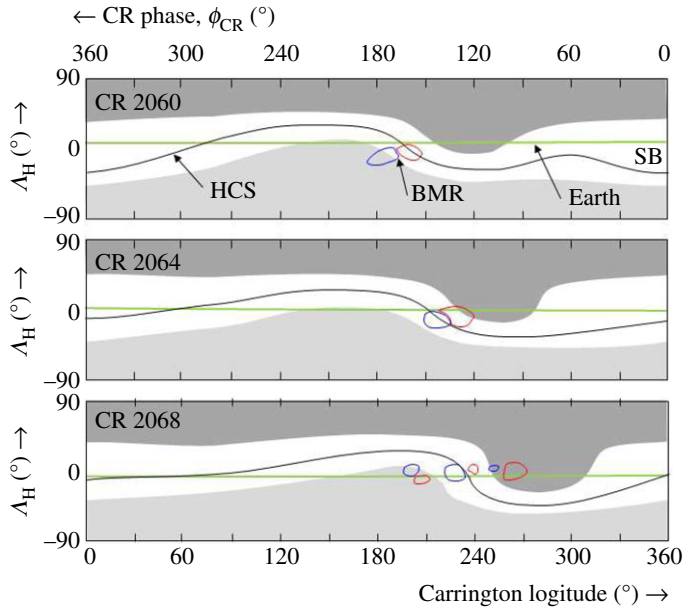
Figure 12. Synoptic maps for Carrington Rotations (CRs) 2060 (top), 2064 (middle) and 2068 (bottom) derived from the Wilcox Solar Observatory magnetograms. In each panel features are plotted as a function of their heliographic latitude, Λ_H, and Carrington Longitude as they rotate through the central solar meridian, as seen from Earth. Carrington Longitude decreases from 360° to zero with increasing CR phase ϕ_{CR} during each CR. The green line gives the Λ_H of Earth and the black line the Heliospheric Current Sheet (HCS, the location of the reversal in the radial field) derived from the photospheric magnetogram at the 'source surface' at the top of the solar atmosphere (at a heliocentric distance r of $2.5R_\odot$ where $R_\odot$ is a mean solar radius) using the PFSS model. The white band is the approximate location of the streamer belt (SB) defined to be between the contours where the (assumed radial) field at $r = 2.5R_\odot$ is ± 2 μT [30]. Also shown are strong ($|B| > 500$ μT) field regions in the photosphere ($r = 1R_\odot$) with radial outward/inward field inside the blue and red contours, respectively. Adjacent regions inside red and blue contours are a Bipolar Magnetic Region (BMR). (Online version in colour.)

V_{SW}. These variations at Earth are explained by the Carrington maps of the solar atmosphere and surface shown in figure 12. These are a combination of magnetic field estimates from the solar photosphere (at a heliocentric distance $r = R_\odot$ where $R_\odot$ is a mean solar radius) and at the nominal solar 'source surface' (at $r = 2.5R_\odot$), the latter being derived from the observed field in the photosphere using the Potential Field Source Surface (PFSS) method which requires a number of assumptions [31].

These maps are based on data from the Wilcox Solar Observatory (WSO) magnetograph. To interpret these magnetograms it must be noted that features are shown at the central meridian of the solar disc and that Carrington latitude decreases with time, and hence also with CR phase ϕ_{CR}, and also that features arrive at near-Earth space after the solar wind propagation time. For a slow solar wind speed of $V_{SW} = 300$ km s^{-1} (typical of the streamer belt) this is of order 140 h which is a lag in CR phase of $\Delta\phi_{CR} \approx 75°$. In fast solar wind emanating from coronal holes (typically $V_{SW} = 700$ km s^{-1}) the lag is of order 60 h ($\Delta\phi_{CR} \approx 33°$) and for the intermediate speed of $V_{SW} = 450$ km s^{-1} seen at the time of the rapid B_X reversal around $\phi_{CR} = 220°$, the lag is close to 93 h ($\Delta\phi_{CR} \approx 50°$). The green line gives the heliographic latitude of Earth and the black line that of the Heliospheric Current Sheet (HCS) where the radial field at the source surface reverses polarity. For example, during CR 2060 the HCS moved rapidly over the Earth at $\phi_{CR} \approx 170°$ which, for a constant $V_{SW} = 450$ km s^{-1}, would give a sharp reversal in B_X at Earth from positive to negative at $\phi_{CR} \approx 220°$: this was duly observed. The warping pattern of the HCS, with a sharp transition from north to south of the Earth (and a gradual return at other Carrington Longitudes) is related

to the emerging field in the photosphere seen the Bipolar Magnetic Regions (BMRs) discussed below. The BMRs are only seen during the three CRs shown in figure 12, but they impress the HCS warp pattern, which is a persistent feature seen during all the CRs studied. Comparison of the three panels of figure 12 shows that the rapid north to south crossing of the HCS, over the projection of the Earth onto the source surface, migrates in ϕ_{CR} from near 170° for CR 2060 to near 130° for CR 2068, a drift in of 5° per CR. Figure 12 also shows that either side of this rapid traversal of the HCS, the Earth dips into faster solar wind outside the streamer belt, firstly to the north of the HCS and then to the south: this is seen in the solar wind data at Earth in figure 11*e* as peaks in V_{SW} either side of the B_X reversal of the HCS crossing.

The motion of the HCS over the Earth from north to south in each CR is rapid and figure 11*e* shows that at this time there is a dip in the solar wind speed for the very fast solar wind seen outside the streamer belt (V_{SW} between about 550 and 700 km s^{-1}) down to intermediate values (to about 450 km s^{-1}), which results from slow solar wind that is pushed forward by the fast solar wind that follows it. The stream–stream interface can be identified in each CR as a strong bipolar signature (not shown) in the tangential solar wind velocity [32,33]. The associated increased solar wind plasma number density, magnetic field and magnetic field structure act as a shield to GCR fluxes [5]. On the other hand, the return sector crossing from south to north of Earth (at $\phi_{CR} \approx 65°$) is much more gradual and falls in a very extended interval during which Earth lies within the streamer belt. This allows the solar wind speed to drop to 250–350 km s^{-1} and consequently there is not as sharp a stream–stream interface due to the more gradual change. This does not form such a strong stream–stream interface and it is much less effective as a GCR barrier. Hence, although the two sector structure generates two peaks and two minima in the solar wind speed, there is just one dominant and persistent GCR shield and so the dominant variation in GCR fluxes is at the period of the solar rotation.

This interval also shows a dominant solar rotation periodicity in the irradiance of Earth by solar electromagnetic radiations. Panels (*f*) and (*g*) of figure 11 show the total solar irradiance contributions caused by sunspot darkening and facular brightening (ΔI_{SS} and ΔI_{fac}, respectively) computed from the magnetograms generated by magnetographs on board the SoHO spacecraft and at Kitt Peak Observatory, using the SATIRE model [34,35]. During CR number 2060 there is some sunspot activity seen as a decrease in the sunspot TSI factor ΔI_{SS} in figure 11*f*. This is caused by a single large spot associated with a single BMR (see top panel of figure 12) that rotates onto the visible disc on 21 August 2007 and off again on 1 September (i.e. is on visible disc for $\phi_{CR} \approx 120$– 240°). During the previous CR this region showed faculae brightening but by CR 2061 the spot has gone and the facular brightening had greatly diminished. Note that the strong warping of the HCS that gives the GCR shield is associated with this BMR.

Irradiance variations remained small until CR 2064 when a sunspot group, including two large spots and surrounding faculae rotated across the disc between 6–16 December 2007($\phi_{CR} \approx 66$– 200°). This is seen in figure 12 and a single BMR which is again at the same Carrington Longitude as the steep warping of the HCS. This longitude is very close to that of the BMR seen four CRs earlier (there is a slight shift to lower ϕ_{CR}, as noted above). Over the three subsequent CRs this region dispersed into faculae (giving a series of declining peaks in ΔI_{fac} but $\Delta I_{SS} \approx 0$ at the same ϕ_{CR} values). Then, again four CRs later, irradiance variability increased in CR 2068, when a longitudinal chain of five spots rotated across the visible disc, the first appearing onto the disc on 24 March 2008, the last rotating off on 4 April ($\phi_{CR} \approx 55$–200°). As for the previous enhancement, over the three subsequent CRs these spots dispersed unto faculae (giving declining peaks in ΔI_{fac} but $\Delta I_{SS} \approx 0$ at the same ϕ_{CR} values). Figure 12 shows that these spots constituted a chain of three BMRs that extend in Carrington Longitude from 190° (where the BMR appeared in CR 2060) to 270° and again straddle the greatest warp in the HCS. The increased longitudinal extent of the sunspot region can be seen in the composite plot of sunspot darkening in figure 11*f*.

Figure 11*h,i* shows that the variation in the brightening caused by faculae in the active regions in the photosphere is mirrored in the brightening of the extension of the same magnetic flux tubes into the chromosphere (plages). Figure 11*i* shows the variation is seen at a wide range of UV wavelengths, as detected by the instruments on the SORCE spacecraft. Figure 11*h* shows an

integral of the irradiance I_{UV} over the wavelength band 190–215 nm which is responsible for the production and heating of ozone in the stratosphere.

The remarkable coherence between the solar rotation oscillations in GCRs, TSI and UV irradiance comes from the fact there is an 'active longitude' effect in the Sun at Carrington Longitudes between about 190 and 270°. This may be because there is greater field intensity in the magnetic flux stored in the overshoot layer beneath the tachocline at these longitudes or/and because some other factor contributes to the stability (or otherwise) of such flux. Three times in the interval, four CRs apart, flux erupts upward through the convection zone and emerges in BRs only at these longitudes. This gives sunspot darkening in that CR, which evolves to enhanced facular brightening of TSI and enhanced UV irradiance as the emerged flux breaks up into smaller flux tubes, the enhancement decaying away over subsequent CRs. The longitudinal restriction of this region gives a marked solar rotation period in the irradiances with enhancements each time the active longitude passes over the solar disc. At the same time, the emergence of these BMRs generates a marked warp of the HCS which gives a strong stream–stream interaction, generating a single GCR shield which makes GCR fluxes rise and fall as it rotates.

References

1. Mironova IA *et al.* 2015 Energetic particle influence on the Earth's atmosphere. *Space Sci. Rev.* **194**, 1–96. (doi:10.1007/s11214-015-0185-4)
2. Gray L *et al.* 2010 Solar influence on climate. *Rev. Geophys.* **48**, RG4001. (doi:10.1029/2009RG000282)
3. Ball WT, Rozanov E, Alsing JA, Marsh DR, Tummon F, Mortlock DJ, Kinnison D, Haigh JD. 2019 The upper stratospheric solar cycle ozone response. *Geophys. Res. Lett.* **46**, 1831–1841. (doi:10.1029/2018GL081501)
4. Gosling JT, Pizzo VJ. 1999 Formation and evolution of corotating interaction regions and their three dimensional structure. *Space Sci. Rev.* **89**, 21–52. (doi:10.1023/A:1005291711900)
5. Rouillard AP, Lockwood M. 2007 The latitudinal effect of corotating interaction regions on galactic cosmic rays. *Sol. Phys.* **245**, 191–206. (doi:10.1007/s11207-007-9019-1)
6. Harrison RG, Nicoll KA, McWilliams KA. 2013 Space weather driven changes in lower atmosphere phenomena. *J. Atmos. Sol.-Terr. Phys.* **98**, 22–30. (doi:10.1016/j.jastp.2013.03.008)
7. Väisänen P, Usoskin I, Mursula K. 2019 Long-term and solar cycle variation of galactic cosmic rays: Evidence for variable heliospheric turbulence. *J. Geophys. Res. Space Phys.* **124**, 804–811. (doi:10.1029/2018JA026135)
8. Gray SL, Harrison RG. 2016 Eclipse-induced wind changes over the British Isles on the 20 March 2015. *Phil. Trans. R. Soc. A* **374**, 20150224. (doi:10.1098/rsta.2015.0224)
9. Takahashi Y, Okazaki Y, Sato M, Miyahara H, Sakanoi K, Hong PK, Hoshino N. 2010 27-day variation in cloud amount in the Western Pacific warm pool region and relationship to the solar cycle. *Atmos. Chem. Phys.* **10**, 1577–1584. (doi:10.5194/acp-10-1577-2010)
10. Plumb RA, Semeniuk K. 2003 Downward propagation of extra-tropical zonal wind anomalies. *J. Geophys. Res. Atmos.* **108**, 4223. (doi:10.1029/2002JD002773)
11. Lockwood M, Bell C, Woollings T, Harrison RG, Gray LJ, Haigh JD. 2010 Top-down solar modulation of climate: evidence for centennial-scale change. *Environ. Res. Lett.* **5**, 034008. (doi:10.1088/1748-9326/5/3/034008)
12. Best CH, Madrigali R. 2016 Evidence of a tidal effect on the polar jet stream. *Ital. J. Eng. Geol. Environ.* **16**, 17–23. (DOI:10.4408/IJEGE.2016-01.O-02)
13. Aplin KL, Lockwood M. 2015 Further considerations of cosmic ray modulation of infrared radiation in the atmosphere. *Astropart. Phys.* **68**, 52–60. (doi:10.1016/j.astropartphys.2015.03.001.)
14. Harrison RG, Nicoll KA, Ambaum MHP. 2015 On the microphysical effects of observed cloud edge charging. *Q. J. R. Meteorol. Soc.* **141**, 2690–2699. (doi:10.1002/qj.2554)
15. Haigh JD. 1994 The role of stratospheric ozone in modulating the solar radiative forcing of climate. *Nature* **370**, 544–546. (doi:10.1038/370544a0)
16. Shindell D, Rind D, Balachandran N, Lean J, Lonergan P. 1999 Solar cycle variability, ozone, and climate. *Science* **284**, 305–308. (doi:10.1126/science.284.5412.305)
17. Hinssen Y, van Delden A, Opsteegh T. 2011 Influence of sudden stratospheric warmings on tropospheric winds. *Meteorol. Z.* **20**, 259–266. (doi:10.1127/0941-2948/2011/0503)

18. Kalnay E *et al.* 1996 The NCEP/NCAR 40-year reanalysis project. *Bull. Amer. Meteor. Soc.* **77**, 437–472. (doi:10.1175/1520-0477(1996)077<0437:TNYRP>2.0.CO;2)

19. Holton JR, Hakim GJ. 2013 *An introduction to dynamical meteorology*, 5th edn. Oxford, UK: Academic Press.

20. Zhang J, Chen H, Li Z, Fan X, Peng L, Yu Y, Cribb M. 2010 Analysis of cloud layer structure in Shouxian, China using RS92 radiosonde aided by 95 GHz cloud radar. *J. Geophys. Res.* **115**, D00K30. (doi:10.1029/2010JD014030)

21. Carslaw KS, Harrison RG, Kirkby J. 2002 Cosmic rays, clouds and climate. *Science* **298**, 1732–1737. (doi:10.1126/science.1076964)

22. Pierce JR. 2017 Cosmic rays, aerosols, clouds, and climate: recent findings from the CLOUD experiment. *J. Geophys. Res. Atmos.* **122**, 8051–8055. (doi:10.1002/2017JD027475)

23. Tinsley BA. 2008 The global atmospheric electric circuit and its effects on cloud microphysics. *Rep. Prog. Phys.* **71**, 066801. (doi:10.1088/0034-4885/71/6/066801)

24. Harrison RG, Ambaum MHP, Lockwood M. 2011 Cloud base height and cosmic rays. *Proc. R. Soc. A* **467**, 2777–2791. (doi:10.1098/rspa.2011.0040)

25. Lam MM, Tinsley BA. 2016 Solar wind-atmospheric electricity-cloud microphysics connections to weather and climate. *J. Atmos. Sol.-Terr. Phys.* **149**, 277–290. (doi:10.1016/j.jastp.2015.10.019)

26. Lockwood M. 2013 Reconstruction and prediction of variations in the open solar magnetic flux and interplanetary conditions. *Living Rev. Sol. Phys.* **10**, 4 . (doi:10.12942/lrsp-2013-4)

27. Lockwood M. 2010 Solar change and climate: an update in the light of the current exceptional solar minimum. *Proc. R. Soc. A* **466**, 303–329. (doi:10.1098/rspa.2009.0519)

28. Carrington R. 1863 *Observations of the spots on the Sun: from November 9, 1853, to March 24, 1861, made at Redhill*, p. 221. London, UK: Williams and Norgate.

29. Mewaldt RA *et al.* 2005 Proton, helium, and electron spectra during the large solar particle events of October–November 2003. *J. Geophys. Res.* **110**, A09S18. (doi:10.1029/2005JA011038)

30. Hoeksema JT, Wilcox JM, Scherrer PH. 1983 The structure of the heliospheric current sheet: 1978–1982. *J. Geophys. Res.* **88**, 9910–9918. (doi:10.1029/JA088iA12p09910)

31. Riley P, Linker JA, Mikić Z, Lionello R, Ledvina SA, Luhmann JG. 2006 A comparison between global solar magnetohydrodynamic and potential field source surface model results. *Astrophys. J.* **653**, 1510–1516. (doi:10.1086/508565)

32. McPherron RL, Siscoe GG, Arge CN. 2004 Probabilistic forecasting of the 3-h ap index. *IEEE Trans. Plasma Sci.* **32**, 1425–1438. (doi:10.1109/tps.2004.833387)

33. Davis CJ, Davies JA, Owens MJ, Lockwood M. 2012 Predicting the arrival of high-speed solar wind streams at Earth using the STEREO heliospheric imagers. *Space Weather* **10**, S02003. (doi:10.1029/2011SW000737)

34. Yeo KL, Krivova NA, Solanki SK, Glassmeier KH. 2014 Reconstruction of total and spectral solar irradiance from 1974 to 2013 based on KPVT, SoHO/MDI and SDO/HMI observations. *Astron. Astrophys.* **570**, A85. (doi:10.1051/0004-6361/201423628)

35. Yeo KL, Krivova NA, Solanki SK. 2014 Solar cycle variation in solar irradiance. *Space Sci. Rev.* **186**, 137–167. (doi:10.1007/s11214-014-0061-7)